Site-Specific Increases in Utero- and Fetoplacental Arterial Vascular Resistance in eNOS-Deficient Mice Due to Impaired Arterial Enlargement 1

Authors: Rennie, Monique Y., Rahman, Anum, Whiteley, Kathie J., Sled, John G., and Adamson, S. Lee

Source: Biology of Reproduction, 92(2)

Published By: Society for the Study of Reproduction

URL: https://doi.org/10.1095/biolreprod.114.123968

BIOLOGY OF REPRODUCTION (2015) **92**(2):48, 1–11
Published online before print 17 December 2014.
DOI 10.1095/biolreprod.114.123968

Site-Specific Increases in Utero- and Fetoplacental Arterial Vascular Resistance in *eNOS*-Deficient Mice Due to Impaired Arterial Enlargement[1]

Monique Y. Rennie,[4,5] Anum Rahman,[4,5] Kathie J. Whiteley,[8] John G. Sled,[2,3,4,5] and S. Lee Adamson[3,6,7,8]

[4]*Mouse Imaging Centre, Hospital for Sick Children, Toronto, Ontario, Canada*
[5]*Department of Medical Biophysics, University of Toronto, Toronto, Ontario, Canada*
[6]*Department of Obstetrics and Gynecology, University of Toronto, Toronto, Ontario, Canada*
[7]*Department of Physiology, University of Toronto, Toronto, Ontario, Canada*
[8]*Lunenfeld-Tanenbaum Research Institute, Mount Sinai Hospital, Toronto, Ontario, Canada*

ABSTRACT

The sites of elevated vascular resistance that impede placental perfusion in pathological pregnancies are unknown. In the current study, we identified these sites in a knockout mouse model (*eNOS*$^{-/-}$) with reduced uterine (−55%) and umbilical (−29%) artery blood flows caused by endothelial nitric oxide synthase deficiency. Uteroplacental and fetoplacental arterial vascular trees of pregnant mice near term were imaged using x-ray microcomputed tomography (n = 5–10 placentas from 3–5 dams/group). The resulting three-dimensional images were analyzed to assess vessel geometry and vascular resistance. In control and *eNOS*$^{-/-}$ trees, ~90% of total uteroplacental vascular resistance was located in the radial arteries. Changes in *eNOS*$^{-/-}$ vessel geometry, including 30% reductions in uterine, radial, and spiral artery diameters, were calculated to increase arterial resistance downstream of the uterine artery by 2.3-fold, predicting a 57% decrease in uterine blood flow. Despite large reductions in *eNOS*$^{-/-}$ spiral arteries (−55% by volume) and maternal canals (−67% by volume), these vessels were relatively minor contributors to resistance. In the *eNOS*$^{-/-}$ fetoplacental tree, the number of arterioles (50–75 μm diameter) increased by 26%. Nevertheless, calculated resistance rose by 19%, predominantly because arteries near the periphery of the tree selectively exhibited a 7%–9% diameter reduction. We conclude that previously observed decreases in uterine and umbilical blood flows in *eNOS*$^{-/-}$ pregnancies are associated with markedly divergent structural changes in the uteroplacental versus fetoplacental circulations. Results showed the radial arteries were critical determinants of uteroplacental resistance in mice and therefore warrant greater attention in future studies in pathological human pregnancies.

endothelial NO synthase, fetoplacental circulation, hemodynamics, microcomputed tomography, placenta, uteroplacental circulation

INTRODUCTION

Placental vascular defects underlie some of the most common and severe pregnancy complications, but the specific location of those vascular defects remains unclear. Preeclampsia is thought to stem from blunted uteroplacental vessel dilation and failure of the spiral arteries to be transformed into wide flaccid tubes [1–3]. Intrauterine growth restriction (IUGR) is thought to stem from a hypovascular fetoplacental tree [4, 5]. Although the full extent of hypovascularity is uncertain, vascular corrosion casts of the fetoplacental vasculature in IUGR pregnancies reveal decreased arterial branching and fewer capillary loops, which are longer and sparsely branched [4, 5]. Clinically, in high risk pregnancies, suspected deficiencies in the placental vasculature are identified via abnormalities in the uterine or umbilical arterial Doppler blood velocity waveforms [4–6]. Waveform abnormalities include a uterine arterial diastolic notch, an umbilical arterial absent or reversed end-diastolic velocity, and elevated waveform pulsatility (e.g., a high resistance or pulsatility index) [4–6]. However, changes in Doppler waveform shape do not reliably reflect changes in vascular resistance nor do they provide information on the specific site of vascular abnormalities in uterine [4, 5, 7] or umbilical circulations [8, 9]. The site of resistance changes in pathological pregnancies and the genetic or environmental factors responsible for these abnormalities remain unknown.

Mouse models present a unique opportunity to understand the distribution of resistance within the placental circulations due to strong structural and cellular similarities to human placentas [10–12], available imaging techniques for characterizing their entire placental vascular bed, and the numerous available mouse models with placental vascular defects. Additionally, uterine and umbilical artery Doppler waveforms in the mouse are comparable to that of the human placenta; both species show similar changes during normal gestational development [13] and in pathologies associated with structural placental vascular anomalies [4–6, 14–16]. Although there are species differences [11], the structure of a single mouse placenta has a fetoplacental vasculature similar to that of a single human cotyledon and a uteroplacental circulation that has radial and spiral arteries similar to the human [12, 17]. A critical difference is the much smaller size of the mouse placenta, which allows the entire placental vascular tree to be imaged in three dimensions via high-resolution microcomputed tomography (micro-CT) [17, 18]. An intact tree is required to maintain tree geometry, which allows calculation of fetoplacental vascular resistance to blood flow [19, 20]. In the mouse placenta, these techniques have revealed site-specific placental vascular defects in several growth-restricted mouse models [19,

[1]Funded by Heart and Stroke Foundation of Ontario Grants NA5804 and T6297 and by Canadian Institutes of Health Research grants FRN: 130403 and FRN: 93618. S.L.A. received salary support as the Anne and Max Tanenbaum Chair in Molecular Medicine at Mount Sinai Hospital.
[2]Correspondence: John G. Sled, Mouse Imaging Centre, Toronto Centre for Phenogenomics, 25 Orde Street, Toronto, Ontario, Canada M5T 3H7. E-mail: jgsled@mouseimaging.ca
[3]These authors contributed equally to this work.

Received: 1 August 2014.
First decision: 27 August 2014.
Accepted: 11 December 2014.

eISSN: 1529-7268 http://www.biolreprod.org
ISSN: 0006-3363

21, 22] and have shown that even subtle changes in the fetoplacental arterial tree can have a large effect on the tree's resistance to blood flow [19, 20]. In contrast, imaging the entire human placental vasculature from umbilical arteries down to the arteriole level has not yet been attempted due to size constraints of both the tissue and the resultant data; to date, micro-CT studies of the human fetoplacental vasculature have been limited to placental biopsies [23, 24].

An important role for the endothelial nitric oxide synthase (*eNOS*) pathway during pregnancy has been well-established in both rodents and humans. Nitric oxide (NO) is a potent vasodilator synthesized by *eNOS* in the endothelium of human uteroplacental [25] and fetoplacental vessels [26], and localized NO levels could have important implications during pregnancy. The activity of *eNOS* in the fetoplacental vessels is lower in human placentas from IUGR pregnancies [27]. Lower levels of *eNOS* in the placental vasculature [28] as well as reduced bioavailability of other members of the L-arginine NO pathway [29] have also been observed in some preeclamptic women, and there is some evidence that administration of L-arginine during pregnancy reduces the incidence of preeclampsia [30]. In pregnant mice lacking *eNOS,* uterine arterial Doppler blood flow pulsatility is abnormally elevated [14], but they do not exhibit other characteristic signs of preeclampsia, including gestational hypertension and proteinurea. However, their fetuses are growth restricted by 10%–20% [14, 31–33], and there is evidence of impaired placental function including placental and fetal hypoxia [14, 33], a blunted gestational rise in end-diastolic umbilical arterial blood velocity [15], and diminished in vivo maternofetal nutrient transport [33]. Furthermore, prior work shows that both the uteroplacental and fetoplacental vasculatures are abnormal in $eNOS^{-/-}$ placentas [14, 15]. Uterine artery blood flow is dramatically reduced (−55%) in $eNOS^{-/-}$ mothers [14] as is uterine artery diameter [14, 34]. Downstream, spiral arteries from $eNOS^{-/-}$ dams are shorter and less coiled than their wild-type (WT) counterparts [14]. Fetoplacental capillary density is reduced as is umbilical artery blood flow (−29%), and both changes are consistent with elevated fetoplacental vascular resistance [15].

The $eNOS^{-/-}$ model is highly relevant to pathological human pregnancies, and it also provides an opportunity to identify sites of changed placental vascular geometry caused by *eNOS* deficiency. Studying this model is also important because of our dearth of knowledge regarding how genes and forces regulate arterial tree structure and how variations in tree structure influence hemodynamic function. In the current study, we hypothesized that changes in geometry would be observed at specific sites within the utero- and fetoplacental arterial trees in $eNOS^{-/-}$ pregnancies and that these changes would result in increased vascular resistance sufficient to explain the decreased uteroplacental and umbilical blood flows previously observed in this model [14, 15]. The goals of the current study were to 1) use micro-CT imaging and analysis to quantify utero- and fetoplacental arterial vascular geometry, 2) determine site-specific vascular defects in the arterial trees of $eNOS^{-/-}$ mice relative to controls, and 3) determine the effect of site-specific defects in geometry on placental vascular resistance.

MATERIALS AND METHODS

Mice

Experimental procedures were approved by the Animal Care Committee of Mount Sinai Hospital and conducted in accordance with guidelines established by the Canadian Council on Animal Care. Homozygous $eNOS^{-/-}$ mice (B6.129P2-Nos3^{tm1Unc}/J; 002684) and WT C57Bl6/J mice (000664, the background strain) were purchased from Jackson Laboratories (Bar Harbor, ME). Males were mated in-house with virgin females of the same strain aged 8–14 wk. The morning that a vaginal copulation plug was detected was designated Embryonic Day 0.5 (E0.5). All the placentas were studied in late gestation at E17.5, that is, before changes associated with parturition, which normally occurs on E19 in C57Bl/6J mice [35].

Injection of Contrast Agent and CT Scanning

The uteroplacental vasculature was perfused with a silicone rubber-based x-ray contrast agent using previously established methods [36, 37]. In brief, pregnant mice at E17.5 were anesthetized with isoflurane, and intracardiac heparin (0.05 ml at 100 international units/ml) was injected and allowed to circulate. A catheter in the descending thoracic aorta was used to clear the lower body vasculature of blood using pump-infused heparinized saline containing xylocaine as a vasodilator [36, 37]. The pump then infused the contrast agent (HV-122 Microfil; Flow Tech Inc., Carver, MA). Infusion was stopped when the bright yellow color of the contrast agent was seen entering the uteroplacental microvasculature of the exposed uterus. After tying off the inferior vena cava, the system was pressurized to 20 mm Hg (i.e., microvascular pressure) while the compound polymerized (see [36] for additional details). We used a pressure appropriate for the microcirculation (e.g., spiral artery pressure ~10–15 mmHg [38], capillary pressure ~20 mmHg [39]) to avoid overpressurization, and potential damage, of the microcirculation while at the same time maintaining the vascular lumens of larger vessels in an open configuration. The uterus was then removed, immersed in formalin, and uterine segments later mounted in agar for micro-CT imaging.

Detailed methods for preparing the fetoplacental vasculature for micro-CT imaging have been described previously [36, 37]. In brief, E17.5 pregnant mice were killed by cervical dislocation, and their uteri were collected into ice-cold phosphate buffered saline (PBS). One by one, the conceptuses were surgically exposed and warmed to resume circulatory function. A cannula inserted into the umbilical artery was first used to clear blood from the vasculature using heparinized saline containing xylocaine [36] and then the contrast agent (MV-122 Microfil) was manually infused until it was seen entering the capillary bed. The umbilical vessels were ligated to maintain pressure during polymerization of the silicone rubber-based contrast agent. The umbilical cord was then severed, placentas immersed in formalin, and they were later mounted in agar for micro-CT imaging.

Three-dimensional datasets were acquired for utero- and fetoplacental contrast-enhanced specimens with the surrounding tissue still intact using an MS-9 micro-CT scanner (GE Medical Systems, London, ON) as previously described [18]. Each specimen was rotated 360° around the vertical axis, generating 720 views that were subsequently reconstructed into data blocks with a 13 μm voxel size. Vascular surface visualizations were generated from micro-CT data to visualize the arterial vasculature as we have described previously [18].

Vascular Segmentation

Uteroplacental vascular trees are difficult to automatically segment due to the unique topology of the tightly packed and coiled spiral arteries. Therefore, uteroplacental micro-CT datasets were manually segmented, slice by slice, to label spiral arteries and maternal canals using the Amira software package (FEI Visualization Sciences Group, Burlington, MA) (Fig. 1). Labeled slices were then reconstructed creating three-dimensional images (Fig. 1). Maternal canal and spiral artery volumes were determined from each segmented dataset. Calipers in the Amira software were used to measure diameters and lengths of uteroplacental vessels. Diameter measurements were made at three or more sites along the imaged segment of the uterine artery, radial arteries, and canals, and at 15 or more sites along the longer and more tortuous spiral arteries. Measurements for each vessel type were then averaged for each specimen examined.

The simpler treelike structure of the fetoplacental arterial vasculature permitted vessel segments and bifurcations to be identified automatically using a segmentation algorithm as described in detail previously [19]. The algorithm returned the center lines of a connected vessel tree and a tubular model for which the lengths, diameters, and connectivity of each vessel segment were known. Measurements of vascular volume, vascular length, vessel segment numbers, and the distribution of vessel diameters were extracted from the resultant tubular models for all vessels >50 μm [19]. The diameter scaling coefficient (the relationship between parent and daughter vessel diameters) was measured for vessels >100 μm due to the variable pattern of branching of the vessels smaller than this diameter [20]. Because the umbilical artery was tied off, its diameter tapered, making automated diameters inaccurate. Therefore, the diameters of umbilical arteries were measured manually with calipers in the Amira software.

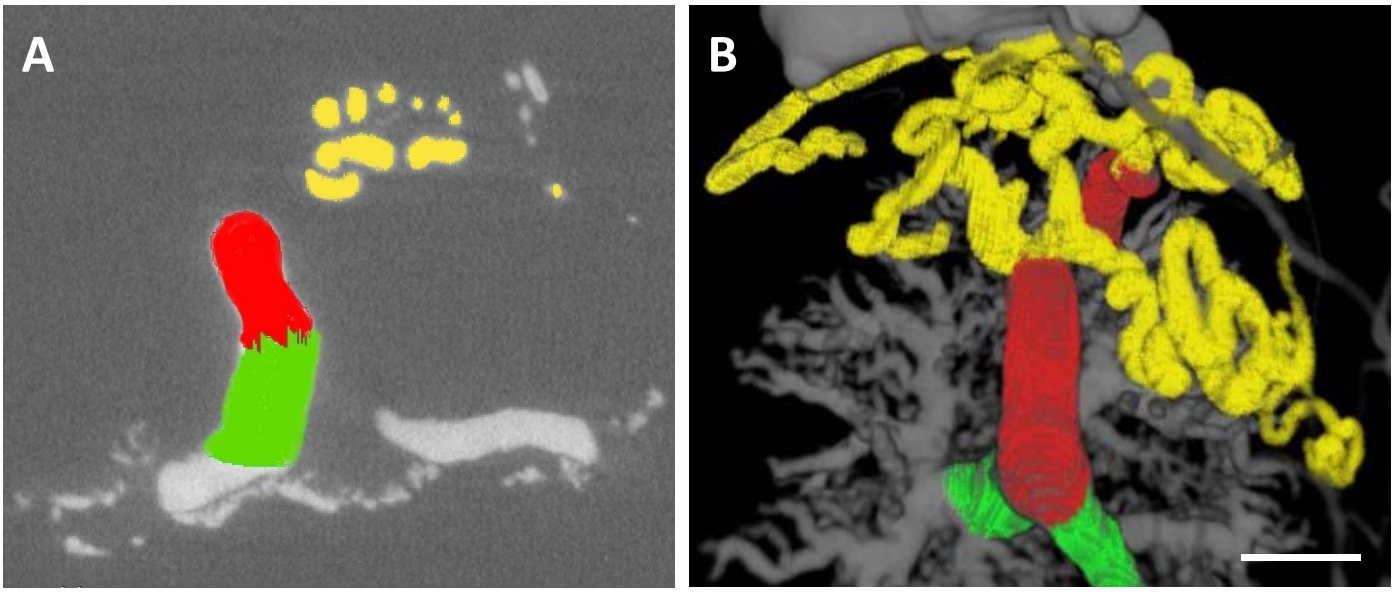

FIG. 1. Manual segmentation of uteroplacental micro-CT datasets. **A**) Example of two-dimensional slice from a three-dimensional micro-CT dataset obtained from a control E17.5 uteroplacental specimen. Slices were manually scrolled through and segmented into spiral arteries (colored yellow), canals (colored red), and canal branches (colored green). **B**) A maximum intensity projection image with segmentation results superimposed to show uteroplacental arterial vessel topology. Maternal blood from radial arteries upstream (not shown) traverses through highly coiled spiral arteries (yellow) that merge into large, trophoblast-lined maternal canals (red). Canals branches (green) direct blood into the maternal labyrinthine blood spaces (grey). Bar = 1 mm, **A** and **B** are at the same scale.

The number of branching generations in each fetoplacental arterial specimen was determined in a downstream direction from the umbilical artery as depicted in Figure 2A. We also used an ordering scheme known as Strahler ordering, which assesses branching in the reverse direction, starting at the smallest vessels. This widely used ordering method is based entirely on how blood vessels connect (i.e., topology). In healthy vascular beds, Strahler order strongly correlates inversely with vessel diameter [40, 41]. Terminal vessel segments were labeled as order 1 and then, tracking upstream, parent vessel segments were assigned 1) the greater of the two orders for the daughter branches or 2) the order of the daughter plus one where the daughters were of the same order (Fig. 2B).

Resistance Calculations

Vascular resistance was calculated based on vessel geometry using standard formulas for resistances in parallel and in series. Resistance calculations assumed 1) laminar flow, 2) Poiseuille's law for flow of fluid through a pipelike structure ($R = 8\eta L/\pi r^4$, where R is resistance, η is viscosity, L is vessel length, and r is vessel radius), 3) equal pressure at each terminal vessel, 4) conservation of mass (flow into a branchpoint is equal to flow out of that branchpoint), 5) a correction factor modeling blood viscosity changes in small vessels derived using adult blood [42], and 6) equations for resistors in series ($R_{total} = R_1 + R_2 + \ldots$) and in parallel ($1/R_{total} = 1/R_1 + 1/R_2 + \ldots$) to calculate total resistance of the arterial supply network. For the fetoplacental vasculature, resistance was determined for each specimen using automatically segmented datasets. For the uteroplacental vasculature, only manually segmented datasets were available, and so instead, the arterial supply to an average WT and average *eNOS*$^{-/-}$ placenta was calculated 1) using average caliper measurements of vessel diameters and lengths to calculate resistance for individual segments using Poiseuille's law and 2) using the average number of radial and spiral arteries and maternal canals for each genotype.

Statistical Analysis

All the data were analyzed using two-way ANOVA to evaluate effects of group and dam. A P-value < 0.05 was considered significant. All the statistical tests were performed using R statistical software (www.r-project.org). Placentas for analysis were selected for technical merit based on complete filling of the arterial vasculature only. For uteroplacental analysis, one to two placentas were analyzed from each of four *eNOS*$^{-/-}$ and five WT dams for a total of seven control and five *eNOS*$^{-/-}$ placentas examined. For fetoplacental analysis, two to four placentas were analyzed from three *eNOS*$^{-/-}$ and four WT dams for a total of eight control and 10 *eNOS*$^{-/-}$ placentas examined. The WT fetoplacental series has been published previously [20]. Two-way ANOVA revealed that variation between dams was not a significant factor so individual placentas were used as the variable n for all the parameters. Results are presented as mean ± SEM.

RESULTS

Phenotype of the Uteroplacental Arterial Tree in eNOS$^{-/-}$ Mice

Dramatic changes were observed in the endothelial-lined vessels of the *eNOS*$^{-/-}$ uteroplacental arterial tree beginning with a 30% reduction in uterine artery diameter relative to controls (Table 1). The uterine artery directly supplied two preplacental radial arteries (Table 1) with similar anatomy found in both groups (Fig. 3). However, the first segment of preplacental radial arteries in *eNOS*$^{-/-}$ mice were shorter (−33%), branching sooner than WT controls, and were smaller in diameter (−27%, Table 1). Preplacental radial arteries in both groups branched one to two times before eventually giving rise to the endothelial-lined spiral arteries (Fig. 3). Spiral artery volume in *eNOS*$^{-/-}$ mothers was 55% smaller than controls (Fig. 4). This reduction in volume was not due to the number of spiral arteries, which was approximately five in each group (Table 1); rather, it was due to decreased spiral artery diameters (−27%; Table 1) and reduced height of the spiral artery region (−17%; Fig. 4D). Spiral arteries converge into large diameter (~400 μm) trophoblast-lined canals (Fig. 3). Canal volume was dramatically reduced in placentas lacking *eNOS* (−67%; Fig. 4). However, this reduction in canal volume was not due to trophoblast-lined canal diameters; canal diameters were unchanged (Table 1). This was in striking contrast to all upstream endothelial-lined vessels (spiral, radial, and uterine arteries), which were smaller in diameter by ~30%. Rather, a significant decrease was observed in height of the canal region (decreased by 19%; Fig. 4D), suggesting a decrease in canal length. Trends toward reduced canal branch volume (10-fold lower, $P = 0.09$) were also observed (Table 1).

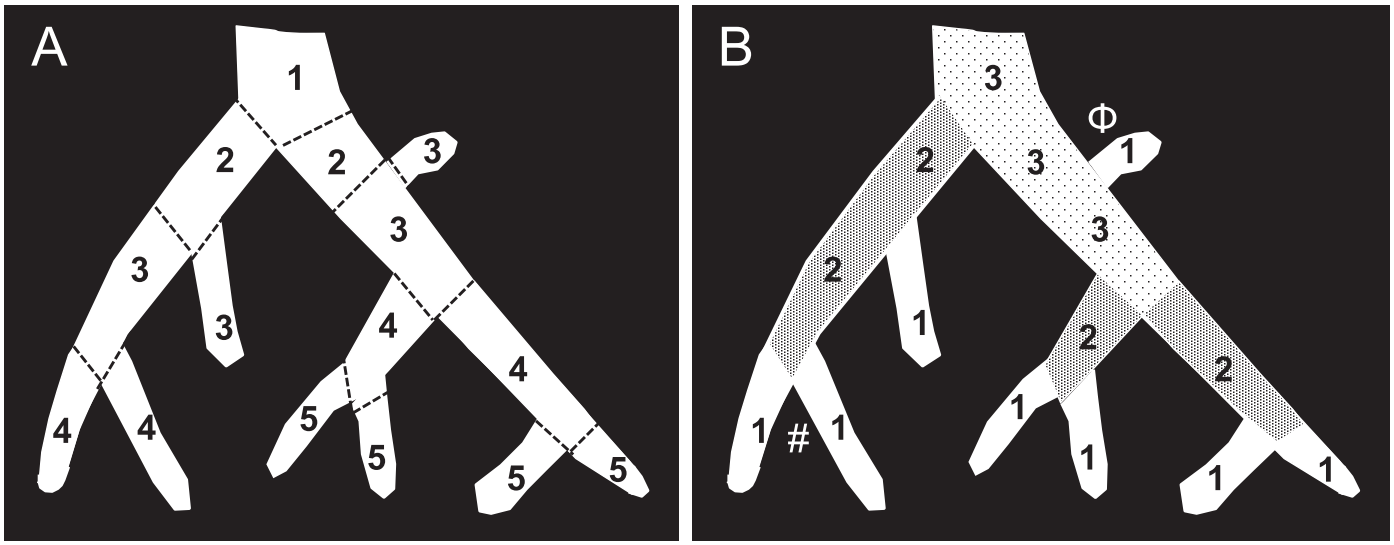

FIG. 2. Branching generation numbers and the Strahler ordering scheme. **A**) Branching generation numbers are labeled on an example vascular tree. The root vessel is labeled as one and, working downstream, branching generation number is increased anytime a branch point is encountered (dashed lines). **B**) The Strahler ordering method is applied to the same example vascular tree. Terminal vessels are labeled as one and parent vessel orders are assigned by working upstream. When two daughter vessels of the same order meet, the parent vessel order is increased by one (e.g., #). When daughter vessel orders differ, parent vessel segments are assigned the maximum order number of the daughter branches (e.g., Φ). The number of Strahler orders in a given tree is usually lower than the number of branching generations, as in this example tree.

TABLE 1. Uteroplacental arterial tree in control and *eNOS*$^{-/-}$ mice.

Parameter	Control[a]	n[b]	*eNOS*$^{-/-}$[a]	n[b]
Uterine artery diameter (mm)	0.234 ± 0.009	3	0.165 ± 0.011**	4
Radial artery diameter (mm)	0.125 ± 0.010	4	0.092 ± 0.006**	5
Spiral artery diameter (mm)	0.197 ± 0.006	7	0.143 ± 0.004**	5
Canal diameter (mm)	0.43 ± 0.03	7	0.44 ± 0.02	5
Number of first order radial arteries	2 ± 0	4	2 ± 0	5
Number of spiral arteries	5.14 ± 0.51	7	4.60 ± 0.75	5
Number of canals	2.71 ± 0.28	7	1.80 ± 0.37	5
Radial artery length (mm)	4.2 ± 0.7	4	2.8 ± 0.2**	4
Spiral artery length (mm)[c]	6.6	7	5.4	6
Canal length (mm)	1.53 ± 0.09	7	1.23 ± 0.05*	5
Presence of canal branches (%)	57%	7	20%	5
Volume of canal branches (mm^3)	0.10 ± 0.04	7	0.01 ± 0.01	5

[a] Data shown as mean ± SEM; group differences denoted by *$P < 0.05$ and **$P < 0.01$.
[b] n = 3 to 7 per group where n indicates the number of placentas examined.
[c] Values obtained from Kulandavelu et al. [14].

Together, these changes in uteroplacental vascularity suggest a generalized reduction in arterial enlargement of endothelial-lined vessels and an overall reduction in elaboration of the uteroplacental circulation.

To determine the physiological effect of reduced vessel diameters in the *eNOS*$^{-/-}$ uteroplacental tree, vascular resistance was calculated for average control and average *eNOS*$^{-/-}$ uteroplacental vasculatures, including the preplacental radial arteries, spiral arteries, and maternal canals. Vasculatures were constructed using group average vessel numbers and dimensions (Table 1). Total resistance in first-order radial arteries, based on two preplacental radial vessels in parallel (Table 1), was calculated to be 7.2 mmHg sec μl^{-1} in the average *eNOS*$^{-/-}$ placenta, 2.2-fold higher than in controls (Fig. 5A). Similar calculations for the average spiral artery bed, based on five spiral arteries in parallel (Table 1) and a previously reported 30% decrease in spiral artery length in *eNOS*$^{-/-}$ [14], revealed a 3-fold increase in resistance in this region of the *eNOS*$^{-/-}$ placenta (Fig. 5A). Canal resistance was negligible at 0.005 mmHg sec μl^{-1}, ~60-fold lower than that of the spiral arteries in both groups (Fig. 5A). When canal, spiral artery, and first-order radial artery resistances were added in series, resistance through this vascular network was 2.3-fold higher in *eNOS*$^{-/-}$ placentas, with altered radial artery geometry being by far the most significant contributor to this resistance elevation (~90%; Fig. 5B). Indeed, resistance at the level of the radial arteries was 10-fold higher than spiral arteries in both control and *eNOS*$^{-/-}$ uteroplacental trees (Fig. 5B).

Phenotype of the Fetoplacental Arterial Tree in eNOS$^{-/-}$ *Mice*

Visualization of the fetoplacental arterial trees at E17.5 showed that in both strains, a centrally located umbilical artery branched across the chorionic plate before elaborately branching into smaller diameter intraplacental arteries. Caliper measurements revealed a small but significant decrease (6%) in umbilical artery diameters in placentas lacking *eNOS* and a significant decrease in the depth of the tree (by 12%) whereas span and total vascular volume did not change significantly

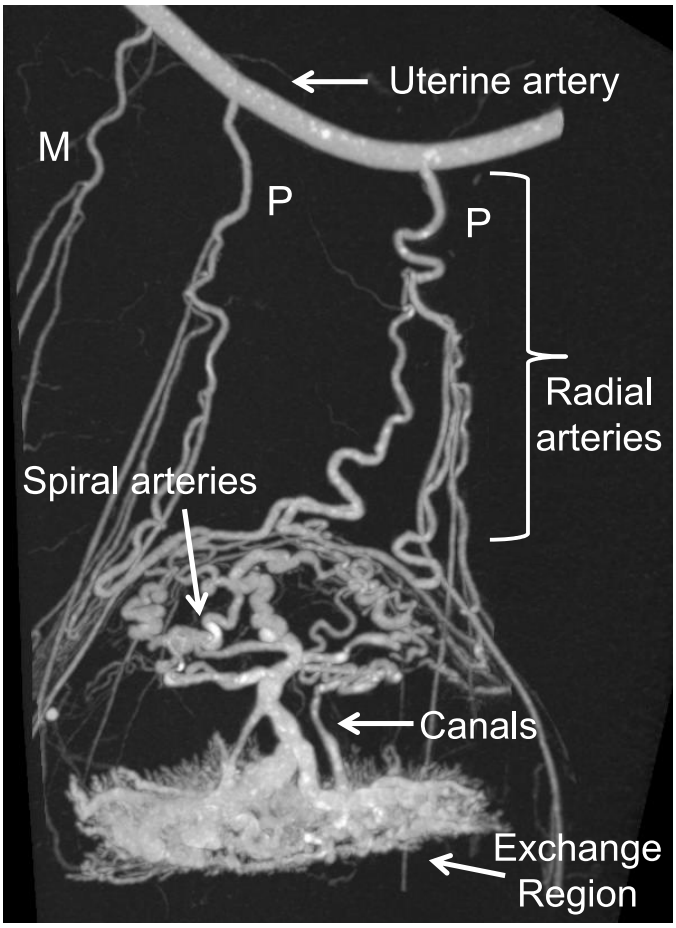

FIG. 3. A maximum intensity projection image of an E13.5 uteroplacental tree. The maternal uterine artery directly supplies two preplacental radial arteries (P) as well as myometrial radial arteries (M) that supply the uterine muscle. This anatomy differs from larger species, including the human and rat, where the uterine artery supplies a circumferential artery known as the arcuate artery from which the radial arteries arise [43]. Preplacental radial arteries penetrate the myometrium to supply larger diameter spiral arteries in the decidua, which converge into the maternal canals that feed the maternal blood spaces of the exchange region. To facilitate imaging the canals, which are embedded within in the junctional zone and labyrinth, only the proximal portion of the exchange region was filled with contrast agent in this study.

(Table 2). Vascular segmentation further revealed that there was a significant increase (+16%) in the total number of arterial vessel segments in placentas lacking *eNOS* (1576 ± 54) compared to controls (1359 ± 61, $P = 0.006$) (Fig. 6). When the cumulative number of vessel segments was plotted as a function of diameter, it was apparent that the increase was confined to smaller diameter vessels (Fig. 6). The numbers of vessel segments were then determined within diameter ranges corresponding to approximate anatomic locations within the tree; chorionic plate arteries >200 μm, intraplacental arteries 75–150 μm, and arterioles 50–75 μm. Arteriole vessel number increased significantly by 26% whereas no significant changes in the number of chorionic plate or intraplacental arteries were observed. The total length of vascular segments in the tree did not differ in *eNOS*$^{-/-}$ mice nor did the total length of the arteriole-sized vessels, though a trend toward increased total length of vascular segments was observed ($P = 0.06$). The length of vessel segments for any given diameter (i.e., the length to diameter ratio) was also unchanged. The diameter scaling coefficient for all vessels >100 μm was significantly increased in *eNOS*$^{-/-}$ placentas (−3.5 in controls vs. −3.21 in *eNOS*$^{-/-}$), indicating that diameters decrease more at each branch point in *eNOS*$^{-/-}$ placentas relative to controls (Table 2).

Interestingly, when the branching structure of the tree was characterized with a Strahler ordering scheme (Fig. 7), all the trees (seven control, eight *eNOS*$^{-/-}$) had exactly 7 orders. This method also revealed an increased number of order 1 to 3 (i.e., small diameter) vessels by ~15% (Table 3). In contrast, the diameters of Strahler order 2 and 3 vessels were significantly decreased by 7% and 9%, respectively ($P < 0.05$), and the lengths of Strahler order 1 and 2 vessels were significantly decreased by 12% and 20%, respectively ($P < 0.01$), in the *eNOS*$^{-/-}$ group (Table 3).

The observed increase in the number of arteriole sized vessels in the *eNOS*$^{-/-}$ placenta would intuitively suggest a decrease in vascular resistance, but when we calculated vascular resistance, we found that it was increased by 19% compared with controls (Table 2). An increase in vascular resistance could result if the additional arterioles formed an extra branching generation (i.e., the vessels were added in series); however, the generation number in the *eNOS*$^{-/-}$ fetoplacental tree was unchanged (Table 2). To test whether the decrease in diameters of arteries in Strahler orders 2 (−7%) and 3 (−9%) was responsible for elevated resistance in the tree, the diameters of order 2 and 3 vessels in *eNOS*$^{-/-}$ placentas were digitally augmented by 7% and 9%, respectively. In this way, the average diameter in these orders was made equal to that of the control group. When resistance was calculated in these diameter-augmented *eNOS*$^{-/-}$ datasets, it was no longer statistically different from controls (0.22 ± 0.03 vs. 0.19 ± 0.01 mmHg sec μl^{-1}).

DISCUSSION

In this paper, we report novel information pertaining to the structure of the uteroplacental vascular tree in mice. Images show that mice, unlike humans and rats [43], have no arcuate artery; possibly, it is unnecessary in mice because of the much smaller size of the uterus. We also report novel information on the physiologically significant effects of *eNOS*$^{-/-}$ on the uteroplacental and fetoplacental circulations. Using high-resolution micro-CT images and vascular segmentation, we generated the first calculations of site-specific resistances throughout the uteroplacental vascular tree. We also used this method to identify the structural changes associated with previously observed reductions in uterine blood flows in a mouse model lacking *eNOS*. We found that vascular resistance at the level of the preplacental radial arteries was ~10-fold higher than at the level of the spiral arteries, and thus radial artery diameter is of paramount importance in determining the total vascular resistance to blood flow through the uteroplacental circulation in both control and *eNOS*$^{-/-}$ placentas. In contrast, in the fetoplacental circulation, we found that slight reductions in diameter in the small arteries of the tree were partially responsible for elevating vascular resistance and reducing umbilical blood flows in *eNOS*$^{-/-}$ mice. In both circulations, we found that abnormalities in arterial geometry in *eNOS*$^{-/-}$ mice predicted physiologically significant increases in vascular resistances.

Similar to previous histological and in vivo microultrasound studies [14, 32], micro-CT imaging showed that uterine artery diameters were reduced by 30% in late-pregnant *eNOS*$^{-/-}$ mice. This appears to be due to blunted pregnancy-induced remodeling because uterine artery diameter does not differ from controls in nonpregnant *eNOS*$^{-/-}$ mice [32]. Indeed,

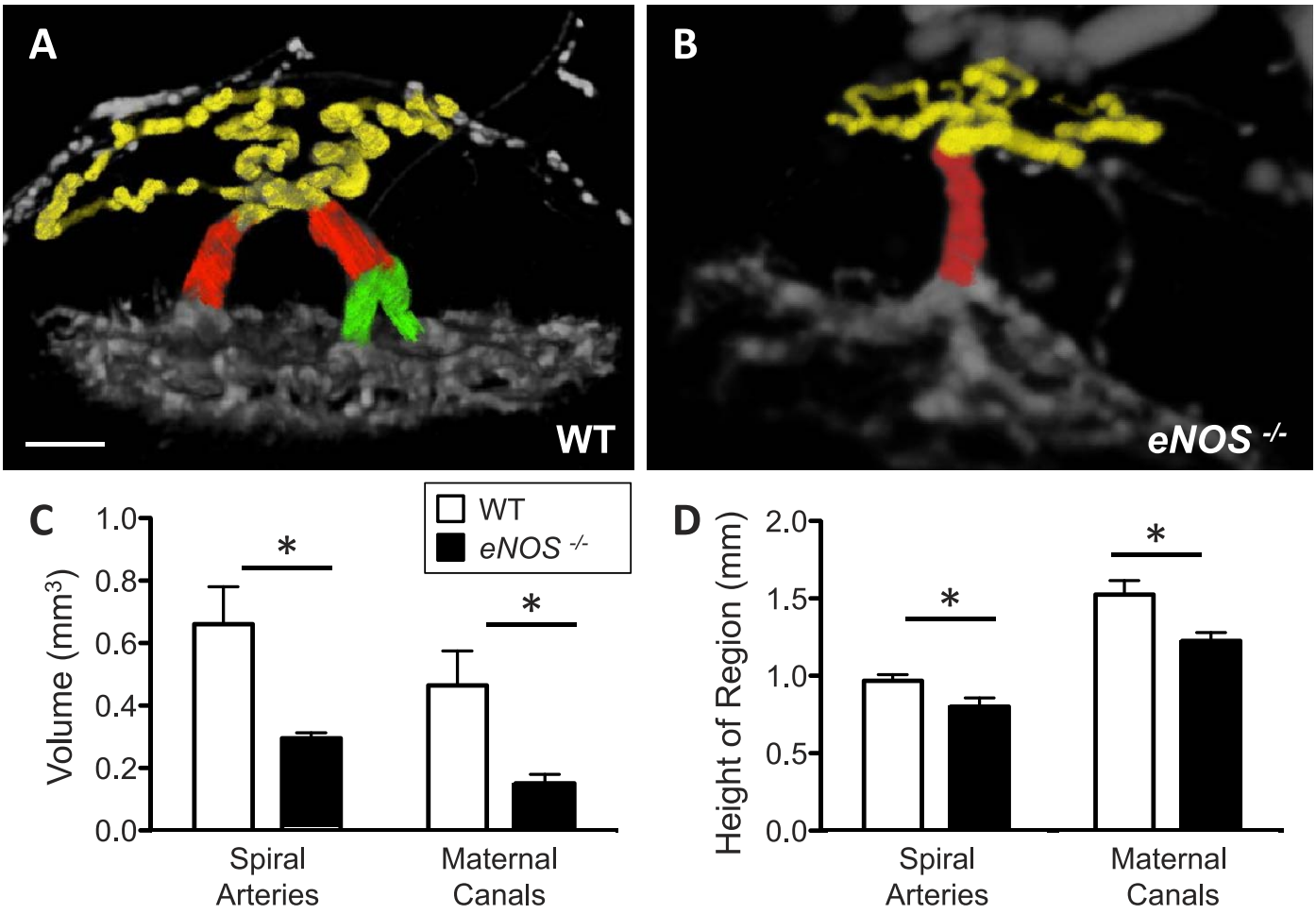

FIG. 4. Uteroplacental vascularity quantified from segmented micro-CT datasets in WT and $eNOS^{-/-}$ mice. Maximum intensity projection images of example control (**A**) and $eNOS^{-/-}$ (**B**) uteroplacental arterial trees; color rendered to depict segmented vessel types. Yellow, spiral arteries; red, maternal canals; green, canal branches. Bar = 1 mm. **C**) Spiral artery volume (yellow in **A**, **B**) was measured from segmented data (n = 7 control and n = 5 $eNOS^{-/-}$ placentas). Total volume of maternal canals was measured from segmented data (volume includes red and green in **A**, **B**). **D**) Height of the region in which spiral arteries were localized was measured from micro-CT isosurface visualizations using calipers in the computer software. Height of the canal region was measured from the location at which spiral arteries converge into canals (yellow meets red in **A**) to where canals or canal branches enter the maternal blood spaces of the exchange region. $^{*}P < 0.05$, group difference determined by ANOVA.

carotid artery diameter [44] and aortic diameter [45] are also unaffected by *eNOS* deficiency in nonpregnant mice as is vascular elasticity of the carotid and femoral arteries [46]. Interestingly, pregnancy-induced enlargement of the aorta is also blunted during pregnancy [45]. We also found a ~30% diameter reduction downstream in the radial arteries. Reduced spiral artery diameter was also observed despite the fact that spiral vessels are not present in the mouse prior to first pregnancy [47] and thus are constructed de novo in pregnancy. Reduced diameters were limited to endothelial-lined vessels; diameters did not differ in trophoblast-lined maternal arterial canals. This is consistent with prior work showing that *eNOS*, which is specifically expressed in endothelium in blood vessels, is a major regulator of vascular remodeling of arteries [48], including the murine uterine artery during pregnancy [32].

Observed changes in vascular geometry downstream of the uterine artery were predicted to increase uteroplacental resistance by 2.3-fold in $eNOS^{-/-}$ placentas. Given that both mean arterial blood pressure in $eNOS^{-/-}$ [45, 49] and maternal hematocrit do not differ from controls during pregnancy [45], the estimated 2.3-fold increase in vascular resistance in $eNOS^{-/-}$ placentas would predict a 57% decrease in flow through this bed. This is remarkably similar to a previously observed ~55% decrease in uterine artery blood flow at this gestational time point [14], suggesting that our calculations account for the majority of the hemodynamically important structural differences between the groups. Thus, changes in resistance based solely on vascular geometry derived from micro-CT images are in tight accord with in vivo measurements of blood flow.

Inadequate spiral artery remodeling is often considered to be a major contributor to elevated uteroplacental vascular resistance in preeclampsia [1–3]. However, like Moll and Kunzel [50], who directly measured pressure in the spiral arteries in rats, guinea pigs, and rabbits, our results indicate that the spiral arteries account for <20% of the resistance of the uteroplacental vasculature. Some human studies also suggest that resistance through the spiral arteries has little impact on total flow [51, 52]. Uterine artery resistance index does not change following delivery of the placenta [51], suggesting a negligible contribution of spiral arteries and the intervillous space to total resistance [51, 52]. The role of radial arteries in dictating uteroplacental vascular resistance has received little attention, despite prior work demonstrating smaller radial artery diameters in preeclamptic women (−17%) [53]. Thus, on the basis of current results and previous work, blunted radial

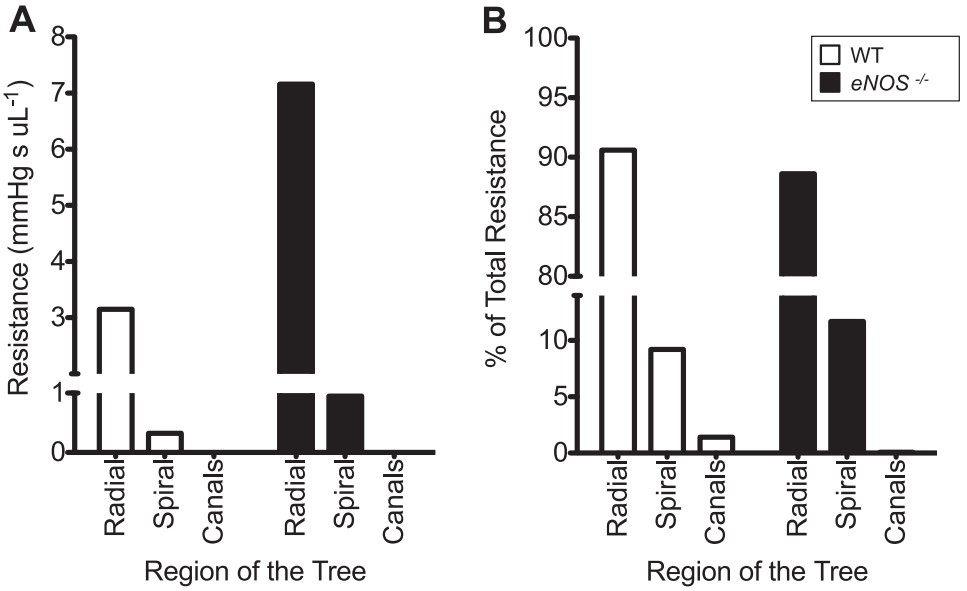

FIG. 5. Resistance in the uteroplacental arterial tree. Vascular resistance of the uteroplacental arterial supply to an average WT (open bars) and average *eNOS*$^{-/-}$ (black bars) placenta was calculated 1) using average caliper measurements of vessel diameters and lengths to calculate resistance for individual segments using Poiseuille's law and 2) using the average number of radial and spiral arteries for each genotype and equations for resistors in parallel to calculate total resistance through that region of the bed. **A**) Vessel type-specific resistances are shown for the radial arteries, spiral arteries, and maternal canals. **B**) The proportion of resistance in each region of the uteroplacental vascular tree was calculated as a percentage of total resistance downstream of the uterine artery. Because calculations were made using group average data, no error bars are shown.

TABLE 2. Geometry of the fetoplacental arterial tree in control and *eNOS*$^{-/-}$ mice.

Parameter	Control (n = 8)[a]	*eNOS*$^{-/-}$ (n = 10)[a]
Measured from raw micro-CT data		
Intravascular volume (mm^3)	2.74 ± 0.16	2.70 ± 0.12
Tree depth (mm)	1.32 ± 0.04	1.17 ± 0.03*
Tree span (mm)	6.66 ± 0.04	6.58 ± 0.07
Umbilical artery diameter (mm)	0.50 ± 0.01	0.47 ± 0.01*
Extracted from segmented datasets		
Number of vessel segments	1359 ± 61	1576 ± 54**
Total length of vasculature (mm)	332 ± 9	333 ± 10
Diameter scaling coefficient (k)	−3.51 ± 0.22	−3.21 ± 0.08*
Length to diameter ratio	2.4 ± 0.6	2.7 ± 0.1
Maximum no. of branching generations	23.7 ± 1.3	24.3 ± 0.4
Number of Strahler orders	7 ± 0	7 ± 0
Arterial resistance (mmHg sec μl^{-1})	0.19 ± 0.01	0.24 ± 0.03*

[a] Data shown as mean ± SEM; group differences denoted by *$P < 0.05$ and **$P < 0.01$ as determined from Tukey post hoc test where n indicates the number of placentas examined.

artery diameter remodeling in preeclamptic women [53] could be responsible for the elevated uterine Doppler resistance indices that are associated with this syndrome [2, 28], and therefore, the radial arteries warrant greater attention in future studies.

Radial arteries were the smallest vessels in the uteroplacental arterial tree, and at less than 100 μm in diameter, they were only slightly larger than Strahler order 2 fetoplacental arterioles. Although our method may underestimate radial artery diameter due to the microvascular pressure of 20 mmHg used for the x-ray contrast agent, there is no question that this level of the uteroplacental circulation is of paramount importance to total uteroplacental arterial vascular resistance. Indeed, we found that only two radial arteries typically branch from the uterine artery to supply each implantation site, so this level of the circulation benefits little from reductions in resistance caused by vessels in parallel. This is in stark contrast to over 200 Strahler order 2 fetoplacental arterioles and likely explains much of the estimated 18-fold discrepancy between uteroplacental arterial resistance and fetoplacental arterial resistance in control placentas (3.42 vs. 0.19 mmHg sec μl^{-1}) predicted by our vascular geometry data.

In contrast to the 30% reductions in diameter of endothelial-lined uteroplacental arteries in *eNOS*$^{-/-}$ mice, the diameter of vessels in the fetoplacental arterial tree in *eNOS*$^{-/-}$ placentas decreased by <10%, even though *eNOS* is expressed in umbilical arterial endothelium, at least in humans [54]. This result suggests that *eNOS* plays a lesser role in control of arterial diameters during growth of the fetoplacental arterial vasculature than during remodeling of the uteroplacental vasculature during pregnancy. Instead, changes in the fetoplacental arterial vasculature in *eNOS*$^{-/-}$ mice were mostly localized to arteriole-sized vessels, which increased in number by 26%. This contrasts with rarefaction of fetoplacental arteriole vessels in fetal growth-restricted human pregnancies [55] but resembles increases in microvascular density observed in placentas from preeclamptic pregnancies [21].

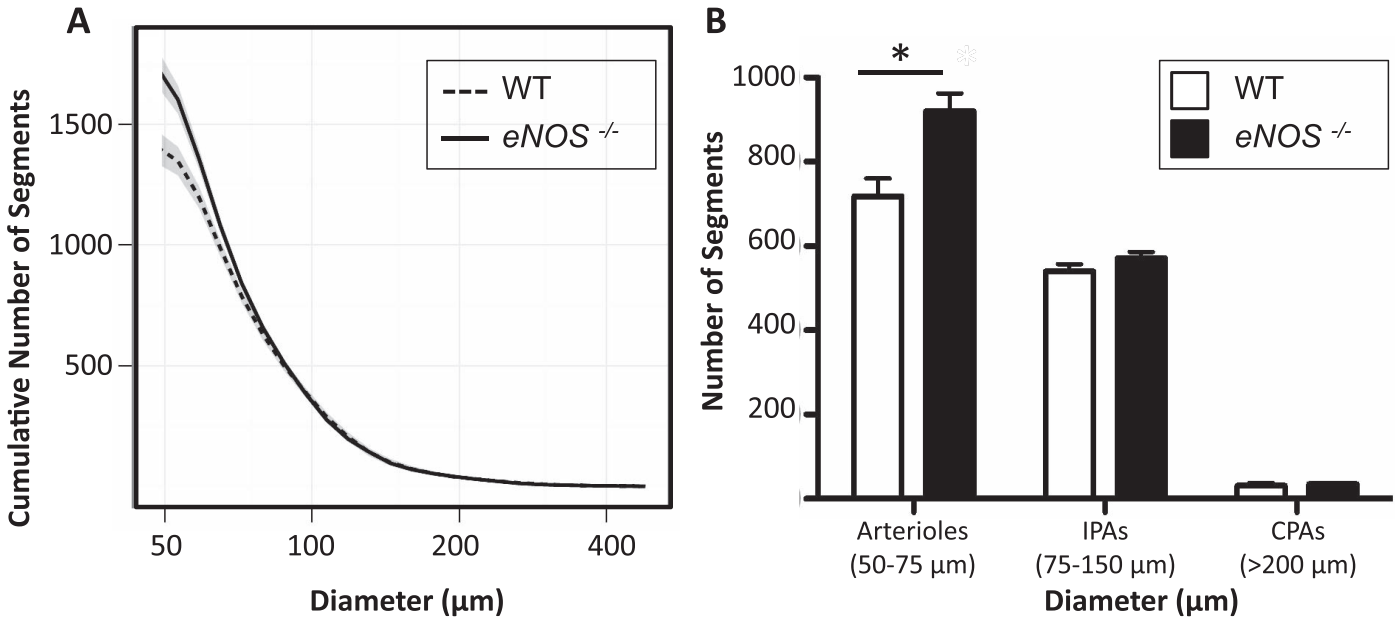

FIG. 6. Distribution of vessel segments. **A**) Cumulative distributions of vessel diameters in WT (dashed line) and *eNOS*$^{-/-}$ (solid line) placentas. **B**) The number of vessel segments within three diameter ranges is shown for WT (open bars) and *eNOS*$^{-/-}$ mice (black bars): arterioles (50–75 μm), intraplacental arteries (IPA, 75–150 μm), and chorionic plate arteries (CPA, >200 μm). Data shown as mean ± SEM. Group differences denoted by $^{*}P < 0.05$ as determined from Tukey post hoc test (n = 8 control and n = 10 *eNOS*$^{-/-}$ placentas).

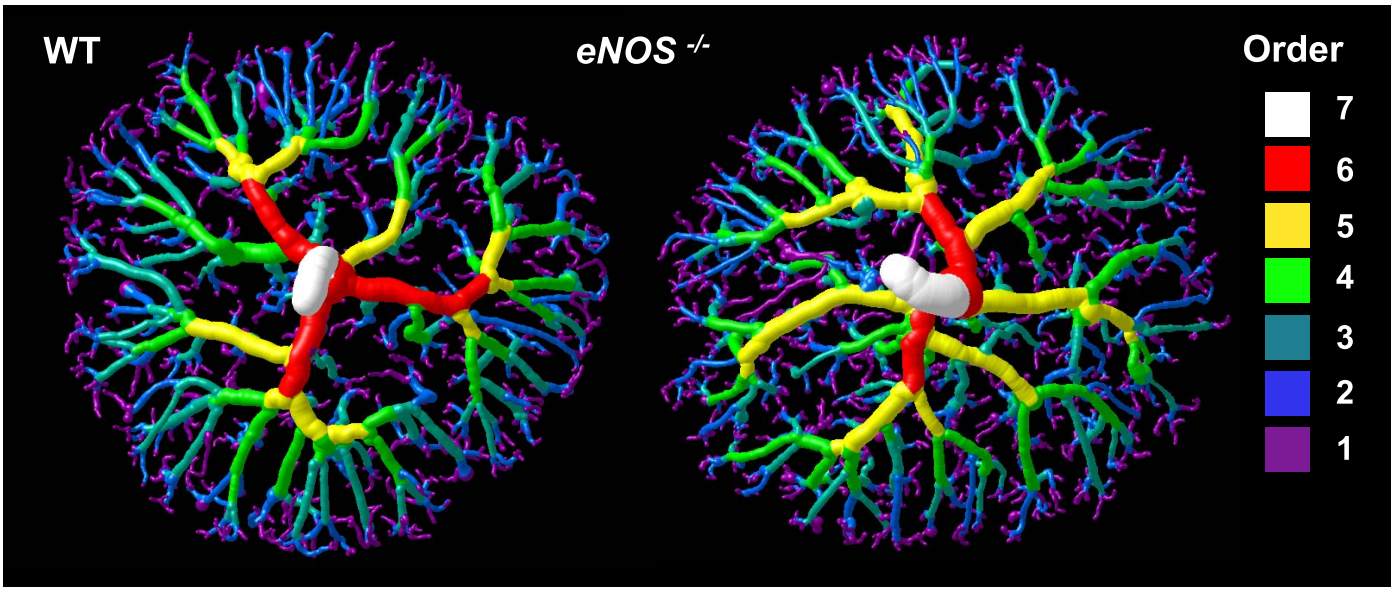

FIG. 7. Strahler ordering of the fetoplacental arterial vascular tree. Colored surfaces depict Strahler order of each vessel in the WT and *eNOS*$^{-/-}$ tree. All the terminal vessels are order 1 and are shown in purple. Order 2 and 3 vessels (dark blue and light blue, respectively) had significantly smaller diameters in the *eNOS*$^{-/-}$ group whereas larger vessels (green, yellow, red, and white) did not significantly differ (n = 8 control and n = 10 *eNOS*$^{-/-}$ placentas).

Interestingly, the elaboration of arterioles found in the *eNOS*$^{-/-}$ placenta also contrasts with the rarefaction of arteriole-sized vessels found in the *eNOS*$^{-/-}$ fetal lung [56], a finding that is consistent with evidence supporting a critical role for *eNOS* in the vasculature of the developing lung [57]. The divergent response in the placenta is consistent with the dramatically lower expression levels of *eNOS* relative to other fetal organs, including the fetal lung and heart, at this gestational age [57]. Because *eNOS* expression in the placenta is already relatively low, it is possible that fetoplacental arteriole elaboration is not a direct consequence of *eNOS* deficiency but is instead secondary to placental hypoxia caused by reduced uteroplacental perfusion in *eNOS*$^{-/-}$ pregnancies [14]. Divergent responses in fetoplacental arteries versus extraplacental arteries may be explained by differences in their intraplacental environment and/or embryological origins. In this regard, it is noteworthy that fetoplacental arteriole-sized vessels (50–75 μm) in the mouse respond to unique branching and guidance cues. Unlike the branching of the larger chorionic and intraplacental arteries of the placenta and of most other arterial trees, the fetoplacental arteriolar branching pattern is not accurately modeled by Murray's law, which results in the

TABLE 3. Strahler ordering of the fetoplacental arterial tree in control and *eNOS*$^{-/-}$ mice.

	Number of elements			Average diameter (μm)			Average length (μm)		
Order	Control[a]	*eNOS*$^{-/-}$[a]	Difference[b]	Control[a]	*eNOS*$^{-/-}$[a]	Difference[b]	Control[a]	*eNOS*$^{-/-}$[a]	Difference[b]
Order 1	736 ± 28	862 ± 41*	15%	63.0 ± 0.1	61 ± 0.1	NS	196 ± 6	175 ± 4*	−12%
Order 2	246 ± 9	287 ± 13*	14%	81.7 ± 0.1	76.3 ± 0.1*	−7%	430 ± 6	355 ± 8	−21%
Order 3	84 ± 4	97 ± 5*	13%	114.1 ± 0.3	104.4 ± 0.1*	−9%	802 ± 34	707 ± 22	NS
Order 4	25 ± 1	30 ± 2	NS	148.8 ± 0.7	138.9 ± 0.5	NS	1006 ± 27	918 ± 50	NS
Order 5	8.0 ± 0.3	8.4 ± 0.4	NS	198.2 ± 1.2	199.5 ± 1.0	NS	1220 ± 102	1427 ± 119	NS
Order 6	2.7 ± 0.2	2.7 ± 0.2	NS	276.3 ± 21.4	275.7 ± 23.9	NS	1661 ± 196	1638 ± 251	NS
Order 7	1.0 ± 0.0	1.0 ± 0.0	NS	501 ± 10	470 ± 11	NS	2485 ± 593	2186 ± 206	NS

[a] Data shown as mean ± SEM for n = 8–10 placentas/group, and group differences denoted by $*P < 0.05$ as determined from Tukey post hoc test.
[b] NS, not significant.

diameter scaling coefficient of approximately −3 [20]. Additional evidence for unique regulation of fetoplacental arteriolar branching comes from *UNC5B*$^{-/-}$ mice, where knocking down the netrin-1 pathway leads specifically to severe rarefaction of the fetoplacental arterioles in *UNC5B*$^{-/-}$ placentas, whereas larger arteries of the fetoplacental circulation and arterioles in organs in the fetal body are unaffected [58]. Thus, hypoxia and/or branching signals unique to the fetoplacental arterioles may be responsible for the observed 26% increase in the number of arteriole-sized vessels in the *eNOS*$^{-/-}$ fetoplacental tree.

Changes in fetoplacental vascular geometry were predicted to increase resistance across the arterial tree by 19% in placentas lacking *eNOS*. The increased arterial resistance was due, at least in part, to smaller diameters in order 2 and 3 vessels because when diameters were digitally augmented in those vessels, arterial resistance was no longer significantly elevated in the *eNOS*$^{-/-}$ tree. Blood viscosity was assumed to be the same in both control and *eNOS*$^{-/-}$ fetuses and was modeled using a correction factor for adult blood viscosity in small vessels [59]. However, fetal red blood cells at this gestational time point are larger than adult cells [60] so fetal blood viscosity may be higher than in adults. Thus, our calculated fetoplacental resistances may be underestimated. Furthermore, blood viscosity in *eNOS*$^{-/-}$ fetuses may be lower than controls because their fetal hematocrit is slightly lower (−12%) [15]. This difference would be predicted to decrease blood viscosity by ~13% [61] in the *eNOS*$^{-/-}$ group. This would be predicted to reduce *eNOS*$^{-/-}$ fetoplacental resistance, thereby reducing the difference in fetoplacental resistance between the groups from 19% to ~11%. If pressures in the umbilical artery and placental capillaries in *eNOS*$^{-/-}$ fetuses are unchanged, then this resistance difference would be predicted to result in an 11% decrease in umbilical flow across the arterial tree, which is much less than the in vivo measured decrement in umbilical blood flow of −29% [15]. The discrepancy is likely due to a significant contribution to vascular resistance in *eNOS*$^{-/-}$ placentas caused by a reduction in placental capillaries [15] and/or by increased resistance in the venous outflow tract, both of which were not imaged and therefore not included in our resistance calculation. This is likely because approximately two-thirds of the total resistance across the placenta is located in the capillaries and venous vessels in mice near term [20]. Thus, reduced intraplacental artery diameters, as well as changes in capillary and/or venous resistances, likely account for the reduction in umbilical artery blood flow in *eNOS*$^{-/-}$ fetuses.

In summary, we used vascular segmentation of micro-CT datasets and computational flow calculations to identify the structural mechanisms responsible for observed reductions in uterine and umbilical artery blood flows in a mouse model lacking *eNOS*. Our findings demonstrate the importance of *eNOS* in both vessel enlargement and vascular arborization of the uteroplacental and fetoplacental circulations. These findings augment our limited knowledge of how genes influence arterial tree structure and how variations in tree structure influence hemodynamic function. In addition, our results further support prior work showing the critical importance of the radial arteries in determining total uteroplacental resistance, and hence blood flow, to the placenta. Together these findings challenge existing dogma on the relative importance of spiral artery remodeling as a determinant of uteroplacental blood flow in normal and pathological human pregnancies.

REFERENCES

1. Meekins JW, Pijnenborg R, Hanssens M, McFadyen IR, van Asshe A. A study of placental bed spiral arteries and trophoblast invasion in normal and severe pre-eclamptic pregnancies. Br J Obstet Gynaecol 1994; 101: 669–674.
2. Matijevic R, Johnston T. In vivo assessment of failed trophoblastic invasion of the spiral arteries in pre-eclampsia. Br J Obstet Gynaecol 1999; 106:78–82.
3. Kaufmann P, Black S, Huppertz B. Endovascular trophoblast invasion: implications for the pathogenesis of intrauterine growth retardation and preeclampsia. Biol Reprod 2003; 69:1–7.
4. Todros T, Sciarrone A, Piccoli E, Guiot C, Kaufmann P, Kingdom J. Umbilical Doppler waveforms and placental villous angiogenesis in pregnancies complicated by fetal growth restriction. Obstet Gynecol 1999; 93:499–503.
5. Krebs C, Macara LM, Leiser R, Bowman AW, Greer IA, Kingdom JC. Intrauterine growth restriction with absent end-diastolic flow velocity in the umbilical artery is associated with maldevelopment of the placental terminal villous tree. Am J Obstet Gynecol 1996; 175:1534–1542.
6. Everett TR, Lees CC. Beyond the placental bed: placental and systemic determinants of the uterine artery Doppler waveform. Placenta 2012; 33: 893–901.
7. Aardema MW, Oosterhof H, Timmer A, van Rooy I, Aarnoudse JG. Uterine artery Doppler flow and uteroplacental vascular pathology in normal pregnancies and pregnancies complicated by pre-eclampsia and small for gestational age fetuses. Placenta 2001; 22:405–411.
8. Adamson SL. Arterial pressure, vascular input impedance, and resistance as determinants of pulsatile blood flow in the umbilical artery. Eur J Obstet Gynecol Reprod Biol 1999; 84:119–125.
9. Adamson SL, Morrow RJ, Langille BL, Bull SB, Ritchie JW. Site-dependent effects of increases in placental vascular resistance on the umbilical arterial velocity waveform in fetal sheep. Ultrasound Med Biol 1990; 16:19–27.
10. Cross JC, Baczyk D, Dobric N, Hemberger M, Hughes M, Simmons DG, Yamamoto H, Kingdom JC. Genes, development and evolution of the placenta. Placenta 2003; 24:123–130.
11. Georgiades P, Ferguson-Smith AC, Burton GJ. Comparative developmental anatomy of the murine and human definitive placentae. Placenta 2002; 23:3–19.
12. Adamson SL, Lu Y, Whiteley KJ, Holmyard D, Hemberger M, Pfarrer C, Cross JC. Interactions between trophoblast cells and the maternal and fetal circulation in the mouse placenta. Dev Biol 2002; 250:358–373.
13. Mu J, Adamson SL. Developmental changes in hemodynamics of the uterine artery, the utero- and umbilico-placental, and vitelline circulations

in the mouse throughout gestation. Am J Physiol Heart Circ Physiol 2006; 291:H1421–428.
14. Kulandavelu S, Whiteley KJ, Qu D, Mu J, Bainbridge SA, Adamson SL. Endothelial nitric oxide synthase deficiency reduces uterine blood flow, spiral artery elongation, and placental oxygenation in pregnant mice. Hypertension 2012; 60:231–238.
15. Kulandavelu S, Whiteley KJ, Bainbridge SA, Qu D, Adamson SL. Endothelial NO synthase augments fetoplacental blood flow, placental vascularization, and fetal growth in mice. Hypertension 2013; 61: 259–266.
16. Venditti CC, Casselman R, Murphy MSQ, Adamson SL, Sled JG, Smith GN. Chronic carbon monoxide inhalation during pregnancy augments uterine artery blood flow and uteroplacental vascular growth in mice. Am J Physiol Regul Integr Comp Physiol 2013; 305:R939–R948.
17. Rennie MY, Sled JG, Adamson SL. Effects of genes and environment on the fetoplacental arterial microcirculation in mice revealed by micro-computed tomography imaging. Microcirculation 2014; 21:48–57.
18. Rennie MY, Whiteley KJ, Kulandavelu S, Adamson SL, Sled JG. 3D visualisation and quantification by microcomputed tomography of late gestational changes in the arterial and venous feto-placental vasculature of the mouse. Placenta 2007; 28:833–840.
19. Rennie MY, Detmar J, Whiteley KJ, Yang J, Jurisicova A, Adamson SL, Sled JG. Vessel tortuousity and reduced vascularization in the fetoplacental arterial tree after maternal exposure to polycyclic aromatic hydrocarbons. Am J Physiol Heart Circ Physiol 2011; 300:H675–H684.
20. Rennie MY, Detmar J, Whiteley KJ, Jurisicova A, Adamson SL, Sled JG. Expansion of the fetoplacental vasculature in late gestation is strain dependent in mice. Am J Physiol Heart Circ Physiol 2012; 302: H1261–H1273.
21. Bainbridge SA, Minhas A, Whiteley KJ, Qu D, Sled JG, Kingdom JCP, Adamson SL. Effects of reduced Gcm1 expression on trophoblast morphology, fetoplacental vascularity, and pregnancy outcomes in mice. Hypertension 2012; 59:732–739.
22. Conroy AL, Silver KL, Zhong K, Rennie MY, Ward P, Sarma JV, Molyneux ME, Sled JG, Fletcher JF, Rogerson S, Kain KC. Complement activation and the resulting placental vascular insufficiency drives fetal growth restriction associated with placental malaria. Cell Host Microbe 2013; 13:215–226.
23. Langheinrich AC, Wienhard J, Vormann S, Hau B, Bohle RM, Zygmunt M. Analysis of the fetal placental vascular tree by X-ray micro-computed tomography. Placenta 2004; 25:95–100.
24. Langheinrich AC, Vorman S, Seidenstucker J, Kampschulte M, Bohle RM, Wienhard J, Zygmunt M. Quantitative 3D micro-CT imaging of the human feto-placental vasculature in intrauterine growth restriction. Placenta 2008; 29:937–941.
25. Nelson SH, Steinsland OS, Wang Y, Yallampalli C, Dong YL, Sanchez JM. Increased nitric oxide synthase activity and expression in the human uterine artery during pregnancy. Circ Res 2000; 87:406–411.
26. Myatt L, Eis AL, Brockman DE, Greer IA, Lyall F. Endothelial nitric oxide synthase in placental villous tissue from normal, pre-eclamptic and intrauterine growth restricted pregnancies. Hum Reprod 1997; 12: 167–172.
27. Krause BJ, Carrasco-Wong I, Caniuguir A, Carvajal J, Farias M, Casanello P. Endothelial eNOS/arginase imbalance contributes to vascular dysfunction in IUGR umbilical and placental vessels. Placenta 2013; 34:20–28.
28. Beinder E, Mohaupt MG, Schlembach D, Fischer T, Sterzel RB, Lang N, Baylis C. Nitric oxide synthase activity and Doppler parameters in the fetoplacental and uteroplacental circulation in preeclampsia. Hypertens Pregnancy 1999; 18:115–127.
29. Lopez-Jaramillo P, Arenas WD, Garcia RG, Rincon MY, Lopez M. The role of the L-arginine-nitric oxide pathway in preeclampsia. Ther Adv Cardiovasc Dis 2008; 2:261–275.
30. Dorniak-Wall T, Grivell RM, Dekker GA, Hague W, Dodd JM. The role of L-arginine in the prevention and treatment of pre-eclampsia: a systematic review of randomised trials. J Hum Hypertens 2014; 28: 230–235.
31. Hefler LA, Reyes CA, O'Brien WE, Gregg AR. Perinatal development of endothelial nitric oxide synthase-deficient mice. Biol Reprod 2001; 64: 666–673.
32. van der Heijden OW, Essers YP, Fazzi G, Peeters LL, De Mey JG, van Eys GJ. Uterine artery remodeling and reproductive performance are impaired in endothelial nitric oxide synthase-deficient mice. Biol Reprod 2005; 72:1161–1168.
33. Kusinski LC, Stanley JL, Dilworth MR, Hirt CJ, Andersson IJ, Renshall LJ, Baker BC, Baker PN, Sibley CP, Wareing M, Glazier JD. eNOS knockout mouse as a model of fetal growth restriction with an impaired uterine artery function and placental transport phenotype. Am J Physiol Regul Integr Comp Physiol 2012; 303:R86–R93.
34. van der Heijden OW, Essers YP, Fazzi G, Peeters LL, De Mey JG, van Eys GJ. Uterine artery remodeling and reproductive performance are impaired in endothelial nitric oxide synthase-deficient mice. Biol Reprod 2005; 72:1161–1168.
35. Mouse Phenome Database. Reproduction Fertility Female. Bar Harbor, ME: The Jackson Laboratory. http://phenome.jax.org/db/qp?rtn=views/measplot&brieflook=44402. Accessed 10 January 2014.
36. Whiteley KJ, Pfarrer CD, Adamson SL. Vascular corrosion casting of the uteroplacental and fetoplacental vasculature in mice. Methods Mol Med 2006; 121:371–392.
37. Rennie MY, Whiteley KJ, Sled JG, Adamson SL. Scanning electron microscopy and micro-computed tomography imaging of the utero- and fetoplacental circulations. In: Croy BA, Yamada AT, DeMayo FJ, Adamson SL (eds.), The Guide to Investigation of Mouse Pregnancy, vol. 1, 1st ed. San Diego, CA: Elsevier; 2014:637–648.
38. Moll W, Kunzel W, Herberger J. Hemodynamic implications of hemochorial placentation. Eur J Obstet Gynecol Reprod Biol 1975; 5: 67–74.
39. Bohlen HG, Gore RW. Comparison of microvascular pressures and diameters in the innervated and denervated rat intestine. Microvasc Res 1977; 14:251–264.
40. Hudetz AG, Conger KA, Halsey JHJ, Pal M, Dohan O, Kovach AG. Pressure distribution in the pial arterial system of rats based on morphometric data and mathematical models. J Cerebral Blood Flow Metab 1987; 7:342–355.
41. Nordsletten DA, Blackett S, Bentley MD, Ritman EL, Smith NP. Structural morphology of renal vasculature. Am J Physiol Heart Circ Physiol 2006; 291:H296–H309.
42. Pries AR, Secomb TW, Gaehtgens P. Biophysical aspects of blood flow in the microvasculature. Cardiovasc Res 1996; 32:654–667.
43. Osol G, Moore LG. Maternal uterine vascular remodeling during pregnancy. Microcirculation 2014; 21:38–47.
44. Quan A, Ward ME, Kulandavelu S, Adamson SL, Langille BL. Endothelium-independent flow-induced dilation in the mouse carotid artery. J Vascular Res 2006; 43:383–391.
45. Kulandavelu S, Qu D, Adamson SL. Cardiovascular function in mice during normal pregnancy and in the absence of endothelial NO synthase. Hypertension 2006; 47:1175–1182.
46. Guo X, Lu X, Ren H, Levin ER, Kassab GS. Estrogen modulates the mechanical homeostasis of mouse arterial vessels through nitric oxide. Am J Physiol Heart Circ Physiol 2006; 290:H1788–H1797.
47. Rennie MY, Mu J, Rahman A, Qu D, Whiteley KJ, Sled JG, Adamson SL. The uteroplacental, fetoplacental, and yolk sac circulations in the mouse. In: Croy BA, Yamada AT, DeMayo FJ, Adamson SL (eds.), The Guide to Investigation of Mouse Pregnancy, vol. 1, 1st ed. San Diego, CA: Elsevier; 2014:201–210.
48. Rudic RD, Sessa WC. Nitric oxide in endothelial dysfunction and vascular remodeling: clinical correlates and experimental links. Am J Hum Genet 1999; 64:673–677.
49. Shesely EG, Gilbert C, Granderson G, Carretero CD, Carretero OA, Beierwaltes WH. Nitric oxide synthase gene knockout mice do not become hypertensive during pregnancy. Am J Obstet Gynecol 2001; 185: 1198–1203.
50. Moll W, Kunzel W. The blood pressure in arteries entering the placentae of guinea pigs, rats, rabbits, and sheep. Pflugers Archiv 1973; 338: 125–137.
51. Schaaps J-P, Tsatsaris V, Goffin F, Brichant J-F, Delbecque K, Tebache M, Collignon L, Retz MC, Foidart JM. Shunting the intervillous space: new concepts in human uteroplacental vascularization. Am J Obstet Gynecol 2005; 192:323–332.
52. Burton GJ, Woods AW, Jauniaux E, Kingdom JC. Rheological and physiological consequences of conversion of the maternal spiral arteries for uteroplacental blood flow during human pregnancy. Placenta 2009; 30: 473–482.
53. Ong SS, Baker PN, Mayhew TM, Dunn WR. Remodeling of myometrial radial arteries in preeclampsia. Am J Obstet Gynecol 2005; 192:572–579.
54. Hracsko Z, Hermesz E, Ferencz A, Orvos H, Novak Z, Pal A, Varga IS. Endothelial nitric oxide synthase is up-regulated in the umbilical cord in pregnancies complicated with intrauterine growth retardation. In Vivo 2009; 23:727–732.
55. Baykal C, Sargon MF, Esinler I, Onderoglu S, Onderoglu L. Placental microcirculation of intrauterine growth retarded fetuses: scanning electron microscopy of placental vascular casts. Arch Gynecol Obstet 2004; 270: 99–103.
56. Han RNN, Babaei S, Robb M, Lee T, Ridsdale R, Ackerley C, Post M,

Stewart DJ. Defective lung vascular development and fatal respiratory distress in endothelial NO synthase-deficient mice: a model of alveolar capillary dysplasia? Circ Res 2004; 94:1115–1123.
57. Teichert A-M, Scott JA, Robb GB, Zhou Y-Q, Zhu S-N, Lem M, Keightley A, Steer BM, Schuh AC, Adamson SL, Cybulsky MI, Marsden PA. Endothelial nitric oxide synthase gene expression during murine embryogenesis: commencement of expression in the embryo occurs with the establishment of a unidirectional circulatory system. Circ Res 2008; 103:24–33.
58. Navankasattusas S, Whitehead KJ, Suli A, Sorensen LK, Lim AH, Zhao J, Park KW, Wythe JD, Thomas KR, Chien CB, Li DY. The netrin receptor UNC5B promotes angiogenesis in specific vascular beds. Development 2008; 135:659–667.
59. Pries AR, Secomb TW. Rheology of the microcirculation. Clin Hemorheol Microcirc 2003; 29:143–148.
60. Kingsley PD, Malik J, Fantauzzo KA, Palis J. Yolk sac-derived primitive erythroblasts enucleate during mammalian embryogenesis. Blood 2004; 104:19–25.
61. Cinar Y, Demir G, Pac M, Cinar AB. Effect of hematocrit on blood pressure via hyperviscosity. Am J Hypertens 1999; 12:739–743.